Polymer Degradation and Stability 208 (2023) 110267

Contents lists available at ScienceDirect

Polymer Degradation and Stability

journal homepage: www.journals.elsevier.com/polymer-degradation-and-stability

Effects of artificial weathering in NR/SBR elastomer blends

Akshay Karekar [a,*], Carsten Schicktanz [b,1], Muhammad Tariq [c,2], Katja Oßwald [d], Katrin Reincke [d], Valentin Cepus [b,d], Beate Langer [b], Kay Saalwächter [a,*]

[a] Institut für Physik, Martin-Luther-Universität Halle-Wittenberg, Betty-Heimann-Str. 7, Halle (Saale) 06120, Germany
[b] Fachbereich Ingenieur- und Naturwissenschaften, Hochschule Merseburg – University of Applied Sciences, Eberhard-Leibnitz-Str. 2, Merseburg 06217, Germany
[c] Institut für Physik, Martin-Luther-Universität Halle-Wittenberg, Von-Danckelmann-Platz 3, Halle (Saale) 06120, Germany
[d] Polymer Service GmbH Merseburg, Geusaer Str. 81f, Merseburg 06217, Germany

ARTICLE INFO

Keywords:
Elastomer blend
Cross-link density
Nuclear magnetic resonance
Residual dipolar coupling
Weathering
Degradation

ABSTRACT

Degradation of polymer blends occurs by the constituent phases undergoing distinct chemical changes that depend on their unique chemical structures. This makes predicting and establishing a structure-property relationship for each phase necessary as well as challenging. In this work, the molecular and physical changes occurring in sulfur-cross-linked natural rubber (NR), styrene–butadiene rubber (SBR), and their 50/50 blend subjected to accelerated weathering are analyzed by ^{1}H nuclear magnetic resonance (NMR) spectroscopy, Fourier-transform infrared (FTIR) spectroscopy, atomic-force microscopy (AFM), and dynamic mechanical thermal analysis (DMTA). NMR transverse relaxation time (T_2) studies suggest the formation of rigid components due to weathering. FTIR and AFM reveal that this is related to the formation of a stiff surface due to chemical modifications, which shows up as an additional thermal transition in the DMTA curves. Low-field double-quantum (DQ) NMR studies of the cross-link density, by the residual dipolar coupling constant (D_{res}), of SBR show a continuous increase in its cross-link density over the weathering duration (988 h). In contrast, NR exhibits dominant chain scission reactions resulting in defects, with both materials demonstrating the formation of different chain lengths. During the first 168 h, NR also undergoes modification of sulfur bond lengths, which is also observed in the blend. The blend largely follows an intermediate trend of cross-link densities compared to the two polymers but shows signs of lesser chain modifications than a weighted average of the two polymers. This is confirmed by phase-resolved DQ magic-angle spinning (MAS) NMR experiments whereby the peak-specific D_{res} of the blend was measured to be less modified than that of the individual vulcanizates, thus proving that the blend is more resistant to weathering than its constituent elastomers.

1. Introduction

In a natural setting, chemical and physical changes of polymeric materials occur due to various environmental stresses like heat, humidity, solar radiation (UV), atmosphere, etc., in a process referred to as weathering [1]. These detrimental factors eventually cause an early failure due to cracking, surface erosion, loss of flexibility, change in color, and breakdown of the chains. In elastomers, the unsaturated bonds are especially prone to these attacks. The susceptibility of aromatic rings to UV has been known, too [2]. The temperature dependence, characterized by an Arrhenius or slightly non-Arrhenius behavior, yields activation energy (E_a) of photodegradation values around 12–20 kJ/mol for aromatic thermoplastics [3] and 27–50 kJ/mol for aliphatic thermoplastics. As much as the extent of weathering a polymer can undergo depends on its chemical structure, the constituent additives present in a polymer composition and the associated thermal history of the polymer system regulate its longevity [1].

The micro- and macrostructural integrity of cross-linked elastomers are directly linked to the density of cross-linking. Generally, a continuous rise in elastic recovery and stiffness is obtained with increasing cross-link density. Properties like tensile and tear strength, toughness, and resistance to fatigue increase up to a particular loading of the cross-linker and reduce gradually thereafter. Studying the network density becomes all the more necessary but tricky when dealing with

* Corresponding authors.
E-mail addresses: akshay.karekar@physik.uni-halle.de (A. Karekar), kay.saalwaechter@physik.uni-halle.de (K. Saalwächter).
[1] This paper is dedicated to the memory of Mr. Carsten Schicktanz, who passed away unexpectedly during the preparation of this work.
[2] Present address: Basic Science Department, University of Engineering and Technology Taxila, Taxila 47040, Pakistan.

https://doi.org/10.1016/j.polymdegradstab.2023.110267
Received 4 November 2022; Received in revised form 6 January 2023; Accepted 10 January 2023
Available online 13 January 2023

technologically and commercially viable polymer systems like elastomer blends. In elastomer blends, differences in the phase-specific cross-link densities can occur by a preferential distribution of the cross-linker in either polymer phase, where migration of the cross-linker across the interfaces can occur. Apart from the extent of reactivity between a curative and an elastomer phase, blend properties such as polymer component ratio, viscosities of the constituent polymers, etc., as well as the mixing procedure, dictate the migration of the additives [4–7]. In blends with phases having largely different curing rates, depletion of cross-linker due to its uptake in the phase with the higher curing rate can induce migration of cross-linker from the other phase, thus depriving the other phase. This results in a cure imbalance and expectedly large differences in the performance of the blend phases and the blend itself. Processes like weathering intensify these differences. All these factors warrant a phase-specific elucidation of cross-link densities for establishing structure–property relationships, and for product development.

The conventional methods of evaluating cross-link density of elastomers by tensile testing (using the Mooney-Rivlin phenomenological equation) [8,9], equilibrium swelling (using the Flory-Rehner equation) [10], and rheology [11] are limited in their applicability when the system involves an elastomer blend. The use of atomic force microscopy (AFM) has also been reported [12] but it lacks a quantitative assessment of the cross-link density.

Perhaps the most important technique for the elucidation of structure and chain dynamics in polymers is nuclear magnetic resonance (NMR) spectroscopy, which has thus been employed for cross-link density measurements in blends. Early phase-resolved studies using NMR involved the measurement of proton line-widths in solvent-swollen blend specimens [13–16]. This approach is qualitative at best, as discussed in recent work by this group [17], in which use of a quantitative alternative was made, as explained below. Using a more direct method, proof of curative migration due to diffusion and solubility in natural rubber and polybutadiene blends has been demonstrated by Klei and Koenig by NMR imaging based upon a Carr-Purcell spin-echo pulse sequence with a gradient magnetic field [18]. The curatives had a higher solubility in polybutadiene and thus resulted in a heterogeneous network.

Cross-link densities in dynamically cured thermoplastic vulcanizates of polypropylene and ethylene–propylene–diene rubber (EPDM) were studied by analyzing the line broadening in single 90° pulse ^{1}H magic-angle spinning (MAS) experiments [19]. In a similar system, qualitative assessments of the cross-link density were made by using different models along with cross-polarization (CP) curves obtained from ^{1}H–^{13}C CP-MAS experiments [20].

In all these latter approaches, the measured results depend upon the through-space orientation-dependent ^{1}H–^{1}H (or ^{1}H–^{13}C) dipole–dipole interaction, which reports on the cross-link density specifically. In a polymer, the spins exhibit a residual dipolar coupling (D_{res}) due to the presence of constraints like entanglements, cross-links, crystallites, etc. that cause incomplete averaging of segmental motions. D_{res} of protons measured under low-resolution conditions has been long used as a measure of cross-link density [21–23], and is connected to the dynamic order parameter (S_b) of the polymer backbone as:

$$S_b = \frac{D_{res}}{D_{ref}} = \frac{3}{5N} \propto \frac{1}{M_c} \tag{1}$$

D_{ref} is polymer-specific coupling whose values for a variety of systems have been reported [24,25], and takes pre-averaging due to fast chain modes within a Kuhn segment into consideration. The equation is a measure of the average molecular weight (M_c, in units of mol/kg) of chains in terms of the number of segments (N) between cross-links or other topological constraints. Through the measurement of D_{res} via a multiple-quantum (MQ) pulse sequence [26], based on the pulse sequence of Baum and Pines [27], this approach has been applied for the measurement of cross-link density and its distribution in complex materials like polyisoprene/polybutadiene (IR/BR) blends [28] and natural rubber/styrene–butadiene rubber (NR/SBR) blends [29]. Though quantitative, a complete distinction of phase-specific cross-link densities could not be established for these systems as the components were made of similar dipolar couplings. This method has also been extended to elastomer/plastic blends of EPDM and ultralow-density polyethylene (ULDPE) blends [30], where a spin–spin relaxation time (T_2) filter was used to suppress the signals arising from crystalline and crystalline–amorphous interface fractions of the ULDPE phase and to obtain cross-link density of the EPDM phase.

In our recent paper [17], a ^{1}H NMR methodology to quantitatively measure the cross-linked density in the individual phases of NR/SBR blends subjected to thermo-oxidative aging was demonstrated. Phase-distinction was achieved by spinning the sample at the magic-angle and using a homonuclear double-quantum (DQ) dipolar recoupling pulse sequence [31].

In the present paper, the role of artificial weathering in the dissimilar aging of NR and SBR phases in their blend is addressed. NR and SBR react differently to oxygen and ozone. SBR itself is composed of randomly bonded aromatic and aliphatic segments. Brown et al. have conducted extensive studies by thermo-oxidative aging and weathering, which show different effects with respect to the aging of NR and SBR in the blend [32,33]. During weathering the high energy UV radiation has been recognized to promote various reactions [34]. Thus, due to their markedly different characteristics, one may expect unique changes in the blend phases that could lead to a distribution of cross-link densities.

The cross-link densities in NR, SBR, and their blend subjected to prolonged weathering are first investigated by a ^{1}H low-field MQ NMR spectroscopy based on the robust pulse sequence introduced earlier. The evolution of cross-link densities of NR and SBR within the blends at different intervals of weathering is quantified through phase-specific studies by ^{1}H DQ MAS NMR spectroscopy using the BaBa-xy16 pulse sequence [31]. The formation of highly constrained fractions due to weathering is evaluated by free induction decay (FID) combined with magic-sandwich echo (MSE)–FID and Hahn-echo T_2 relaxometry, which is suitable to quantify solid-like components with dipolar couplings too strong for the above-mentioned technique. Further, the changes in the materials are chemically investigated by Fourier-transform infrared (FTIR) spectroscopy. Lastly, to get a physical perspective, dynamic mechanical thermal analysis (DMTA) and atomic force microscopy (AFM) are employed for probing the macroscopic and microscopic moduli, respectively.

2. Experimental section

2.1. Sample preparation

2.1.1. Materials

Compounds of NR, SBR, and NR/SBR blend (50/50 ratio by parts per hundred rubber, phr) were prepared using the composition reported in a previous work [17]. Solution-polymerized styrene−butadiene rubber (grade SPRINTAN SLR 4602-Schkopau, $T_g = -25$ °C) was supplied by Trinseo Deutschland GmbH (now Synthos Schkopau GmbH, Schkopau, Germany). This is composed of 21.1 % styrene and 62.1 % of the vinyl copolymer 1,2-polybutadiene. Thus, 1,4-polybutadiene constitutes 16.8 % of the rubber. Natural rubber (grade SMR10, $T_g = -60$ °C) was supplied by Weber and Schaer GmbH & Co. KG (Hamburg, Germany). NR was masticated by 10 passes over a two-roll mill before use in formulations.

The three compounds were formulated based on a conventional vulcanization system consisting of 2.5 phr sulfur (Carl Roth GmbH, Germany) and 1.5 phr n-cyclohexyl-2-benzothiazole sulfenamide (CBS) accelerator (TCI Deutschland GmbH, Germany), along with 1 phr stearic acid (Carl Roth GmbH, Germany) and 3 phr zinc oxide (Carl Roth GmbH, Germany) activators. The raw materials were mixed for 10 min at 50 °C and a rotor speed of 50 rpm in a Haake Rheomix 600p (Thermo Scientific, Germany) lab-scale internal mixer to a fill factor of 0.7. The mixed

compounds were cross-linked into 2 mm thick plates on a hydraulic press based on their 90 % curing times (t_{90}) of 4, 8, and 22 min for NR, SBR, and the blend, respectively, obtained according to DIN 53529 on an Elastograph MDR (Göttfert, Germany) moving-die rheometer. For comparative studies, pristine polymers with similar thermal histories were also prepared.

2.1.2. Weathering

Accelerated weathering was performed according to ISO 4892–2 (2013) Method A, Cycle 1 in a Q-SUN Xe-2 rotating rack xenon arc test chamber (Q-Lab Corporation, USA) equipped with a Xenon arc lamp emitting light equivalent to direct sunlight (Daylight-Q) using a silica glass filter. Rectangular specimens (100 × 10 × 2 mm^3) were fixed on specimen holders by clamping the ends. These holders were then mounted on the rotary rack and subjected to an irradiation of 60 ± 2 W/m^2 in the range of 300 nm and 400 nm. The radiation exposure corresponded to an energy of about 213 MJ/m^2.

The specimens were subjected cyclically to light for 102 min followed by a spray cycle of 18 min by reverse-osmosis deionized water for a total exposure duration of 988 h. The chamber was maintained at a temperature of 38 ± 3 °C and a relative humidity of 50 ± 10 %, with the black-standard temperature at 65 ± 3 °C. Samples were picked at durations of 72, 168, 504, and 988 h of weathering for analyses.

2.2. Methods

2.2.1. Dynamic mechanical thermal analysis (DMTA)

Dynamic mechanical properties were measured in air in the torsion mode on an ARES-G2 (TA Instruments, USA). Specimens with a width of 10 mm and a thickness of 2 mm were mounted. The specimens were pre-stretched by an axial force of 0.2 N before cooling down to −80 °C using a chiller. Following a soaking time of 5 min, a temperature ramp was performed up to 100 °C at a ramp rate of 5 K/min. Strain amplitude and frequency were set to 1 % and 1 Hz, respectively.

2.2.2. AFM nanoindentation measurements

For AFM nanoindentation experiments, the atomic force microscope NanoWizard 4 from JPK instruments (Germany) was used. Measurements were performed in contact mode using NSC 15 cantilevers, purchased from Mikromasch, with a nominal spring constant of 40 N/m and resonance frequency of 325 kHz, and a silicon tip with a radius of 8 nm, full tip cone angle of 40°, and tip height 12–18 μm (manufacturer's data). The employed cantilevers were calibrated using the contact-free method.

In AFM indentation, the tip of the AFM cantilever is brought into contact with the sample surface using a *z*-piezoscanner and pressed into the surface. The corresponding applied force is measured as a function of tip displacement, thus generating a force-distance curve. After the approach cycle, the tip is retracted back to its rest position. The indentation depth can be calculated as the *z*-piezoscanner displacement minus the cantilever deflection [35]. For all the measurements, a constant tip speed of 2 μm/s was set. More than 50 indentation measurements were performed at different spots of the core region as well as of the skin region across the cut surface of the weathered sample. A similar number of measurements was also carried out on an unexposed sample. The suitable spots for the measurements were selected by first imaging the surface of the sample in the tapping mode of AFM operation. Selected spots were lying on locally flat areas and far from any grooves or adjacent walls/structures.

Samples for AFM measurements were prepared by microtomy using liquid nitrogen. Slices (size ≈ 2 × 2 mm^2) of the samples were obtained by cutting a thin cross-section from the center of the sample bar (80 × 10 × 2 mm^3). The obtained slices were then placed on freshly cleaned silicon (Si/SiO_2) substrates. Measurements on the skin region were performed within about 30 μm from the directly exposed face, whereas the measurements on the core region were performed at the central part of the slice.

2.2.3. FTIR spectroscopy

The FTIR spectroscopic investigations were conducted on a Bruker Vertex 70 FTIR spectrometer (Germany) equipped with a Platinum ATR cell and connected to a Hyperion 2000 IR microscope with a 15 X Cassegrain objective. IR spectra of the skin and the core of the specimens were recorded at a resolution of 4 cm^{-1} from 4000 to 600 cm^{-1} using the ATR cell. IR microscopic mappings were recorded in the same spectral range in reflectance mode, processed with Kramers-Kronig transformation to extract absorbance information, and represented as Gram-Schmidt integral in a pseudo-color representation.

The sample stripes were fixed in Micro Vice Clamps equipped with SliceIR Clamps (both S.T. Japan) and were cut with a fresh razor blade at an angle of 90° for IR microscopy.

2.2.4. Static low-field time-domain ^1H NMR spectroscopy

Experiments were performed on a Bruker minispec mq20 (Germany) benchtop spectrometer having a magnetic field strength of approximately 0.5 T, which corresponds to a resonance frequency of 19.95 MHz. Small discs were punched from the weathered specimens and stacked in a 10 mm NMR tube up to a height of 6 mm. A Bruker BVT 3000 temperature controller was used to maintain a constant measurement temperature of 80 ± 0.1 °C. The 90° pulse length and receiver dead time corresponded to 2.6 μs and 11 μs, respectively. The recycle delay ($5T_1$) for the pristine, unexposed, and weathered samples were determined to be about 0.6 s for NR and 0.2 s for SBR.

2.2.5. High-field ^1H DQ MAS NMR spectroscopy

Chemically (phase-resolved) measurements were performed on a Bruker Avance III (Germany) spectrometer with a magnetic field strength of 9.4 T, which corresponds to a resonance frequency of 400 MHz. A 1 mm thick rubber ring (3 mm outer diameter and 2 mm inner diameter) was packed at the center of a 4 mm zirconia rotor with a Vespel® rotor cap. The sample was held in position by polytetrafluoroethylene spacers on either side. A Bruker BVT 3000 temperature controller was used for measurements at 80 ± 0.1 °C. The 90° pulse corresponded to a length of 2.5 μs at a pulse power of 54 W.

3. NMR theory

3.1. Spin–spin relaxation time (T_2) measurements

Also known as the transverse relaxation time, T_2 can be used to quantitatively distinguish the amounts of different fractions based on the ease of their segmental mobility within a specimen. In a weathered specimen, the stiff, tightly cross-linked, and/or oxidized fractions can be separated from the moderately cross-linked mobile regions and the fast-moving defects (in cross-linked rubbers these are the loops, dangling chain-ends, and sol fractions that are mechanically inelastic). In a T_2 sense, rigid (possibly glassy) fractions formed due to shorter chain segments have a faster relaxation decay (shorter T_2), whereas the others have slower relaxation decay (longer T_2). The most constrained fractions, in this case, the regions closer to the irradiated surface, are associated with a rigid-limit coupling between the protons as high as about 30 kHz. This translates to a T_2^{eff} (effective T_2) of about 20 μs for the stiff/rigid components of the surface and underneath. The corresponding shape parameter (β_r) of the rigid fractions in a multicomponent modified-exponential decay fitting function ($\propto f_x \exp[-(t/T_{2,x}^{eff})^{\beta_x}]$) takes a value of 2 (Gaussian decay) in this case. Measuring the rigid fraction (f_r) by an FID experiment (by a single 90° pulse) alone leads to underestimated results due to a loss in the initial decay signal owing to a longer receiver dead time (RDT, see Fig. S1 in Supporting Information). It is 11 μs for the low-field spectrometer used in these studies. The loss in the initial part of the signal can be compensated by performing the

pulsed version of the magic-sandwich echo (MSE) experiment that performs a time-reversal by refocusing multispin dipolar interactions of the decay signal [36]. The signals from both these experiments can be simultaneously fitted to obtain the relevant fractions and their respective transverse relaxation times [37]. Slowly decaying components having relatively larger mobility are also probed by stitching a Hahn-echo signal to the FID. Fig. S1 in the Supporting Information illustrates this and the role of MSE-FID for NR and SBR weathered up to 988 h.

A three-component fitting function is required to completely gage these samples. Due to the higher number of data points obtained in an FID experiment, a 10 % weighting is applied. The three fractions obtained are: a rigid fraction due to tightly cross-linked or oxidized (due to weathering) regions, a second fraction that is representative of the majority of the vulcanizate's volume composed of relatively softer components of moderate cross-linking, and a third fraction consisting of the (mobile) defect fraction. A detailed discussion can be found in Section 4.3.2.

3.2. Static low-field time-domain ^1H MQ-NMR

As introduced earlier, cross-link densities on a low-field spectrometer are measured using an MQ pulse sequence [26]. The method has been detailed elsewhere [38] and is therefore described here only very shortly. The experiment yields two signals as a function of pulse sequence duration, τ_{DQ}: a double quantum signal (I_{DQ}) and a decaying reference signal (I_{ref}). I_{DQ} results from contributions of coupled spins at shorter times. I_{ref} also contains a contribution from uncoupled spins (defects) that behave isotropically. A sum MQ signal ($I_{\Sigma MQ} = I_{ref} + I_{DQ}$) is a fully dipolar refocussed signal that decays due to molecular motions. In networks, this decay is found to be nearly equal to that of an I_{DQ} signal. This enables the removal of the effects of molecular motions from I_{DQ} through normalization by a point-by-point division, satisfying the condition: $I_{nDQ} = I_{DQ}/(I_{\Sigma MQ}$ - defects). The resulting normalized DQ (nDQ) signal, I_{nDQ}, is an inverted dephasing curve that reaches a 0.5 intensity limit upon optimum removal of the defect fraction. The defect fraction can be normally described using a single- or bi-exponential decay function [39]. The resulting nDQ build-up curve is a network-structure-only quantity and is independent of temperature, as long as it is measured far above T_g.

The fitting function to this build-up curve is a numerical integral assuming a log-normal distribution of coupling constants ($\ln(D_{res})$) [40]. The Abragam-like kernel function [41], shown in Eq. (2), is suitable to describe data taken on homogeneous rubbers based upon homopolymers without long side chains.

$$I_{nDQ}(\tau_{DQ}, D_{res}) = 0.5\left[1 - \exp\left\{-(0.378\epsilon D_{res}\tau_{DQ})^{1.5}\right\} \times\cos(0.583\epsilon D_{res}\tau_{DQ})\right] \quad (2)$$

For this static experiment, the efficiency factor $\epsilon = 1$. τ_{DQ} is the instantaneous DQ evolution time for the respective point in the I_{ref} and I_{DQ} signals, both of which decay at longer τ_{DQ}. The log-normal probability distribution function of residual couplings, $P(\ln(D_{res}))$ reads:

$$P(\ln(D_{res})) = \frac{1}{\sigma_{ln}\sqrt{2\pi}}\exp\left[-\frac{\{\ln(D_{res}) - \ln(D_{med})\}^2}{2\sigma_{ln}^2}\right] \quad (3)$$

It provides the average D_{res} as a median value (D_{med}) and a logarithmic distribution width (σ_{ln}). The standard deviation is a positive and dimensionless quantity, where $\sigma_{ln} = 0.5$ corresponds roughly to a half-decade-wide distribution. For narrow distributions, the build-up curve can be approximated by an inverted Gaussian, and the cross-link density (D_{med}) is encoded in its initial slope.

3.3. Phase-resolved high-field ^1H DQ MAS NMR

The broad and featureless spectrum of a solid sample in a static experiment can be improved by spinning it at moderately high frequencies in a MAS experiment. A demonstration of this can be seen in Fig. 1 for the three unaged samples of cross-linked NR, SBR, and the 50/50 blend, one-dimensional spectra of which are obtained after Fourier transformation of the respective FIDs following a 90° pulse. Thus, MAS yields high-resolution spectra for phase-specific studies.

The cross-link densities in this case can be measured by obtaining build-up curves in a 2D fashion using the BaBa-xy16 pulse sequence. Like the static MQ experiment discussed earlier, this DQ MAS experiment yields the typical I_{DQ} and I_{ref} signals, which can be obtained by taking one-dimensional projections of every two-dimensional resonance peak of interest. The rotor-synchronized pulse sequence facilitates obtaining points at every rotor period. However, for these studies, signals at every even multiple of the rotor period were measured.

The fitting function is based on that used for the static measurements. The quantum mechanical treatment of this experiment gives the efficiency factor in the kernel function (Eq. (2)) that is reduced to $\epsilon = 0.78$ [31].

4. Results and discussion

4.1. Macroscopic moduli

Weathering brings about physical and chemical changes in the exposed specimens. The cyclic water sprays cause cooling and shrinking of the specimen, whereas UV irradiation leads to heating and expansion. The resulting expansion and contraction lead to specimen deformation and cracks formation and their propagation. This aspect is discussed in more detail in Section 4.3.1.

The DMTA experiments give a first indication of the bulk changes occurring in the weathered samples. The storage and loss modulus (G' and G'', respectively) obtained from temperature ramps of NR and SBR samples subjected to various durations of weathering are shown in Fig. 2. Below T_g, NR reveals a reduction in modulus with the exposure duration. With an increase in the temperature, the 72 and 168 h weathered specimens demonstrate identically marginal retention of G', indicating hardening compared to the unaged specimen. Thus, a

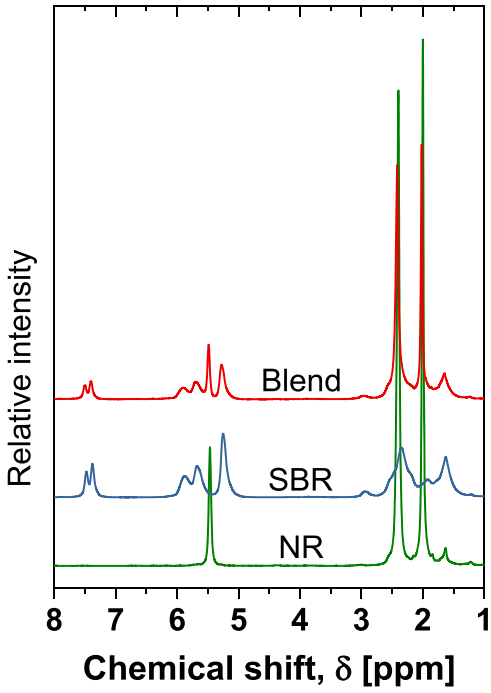

Fig. 1. Chemically resolved peaks in ^1H spectrum of cross-linked NR, SBR, and the blend. (Adapted from Ref. [17]).

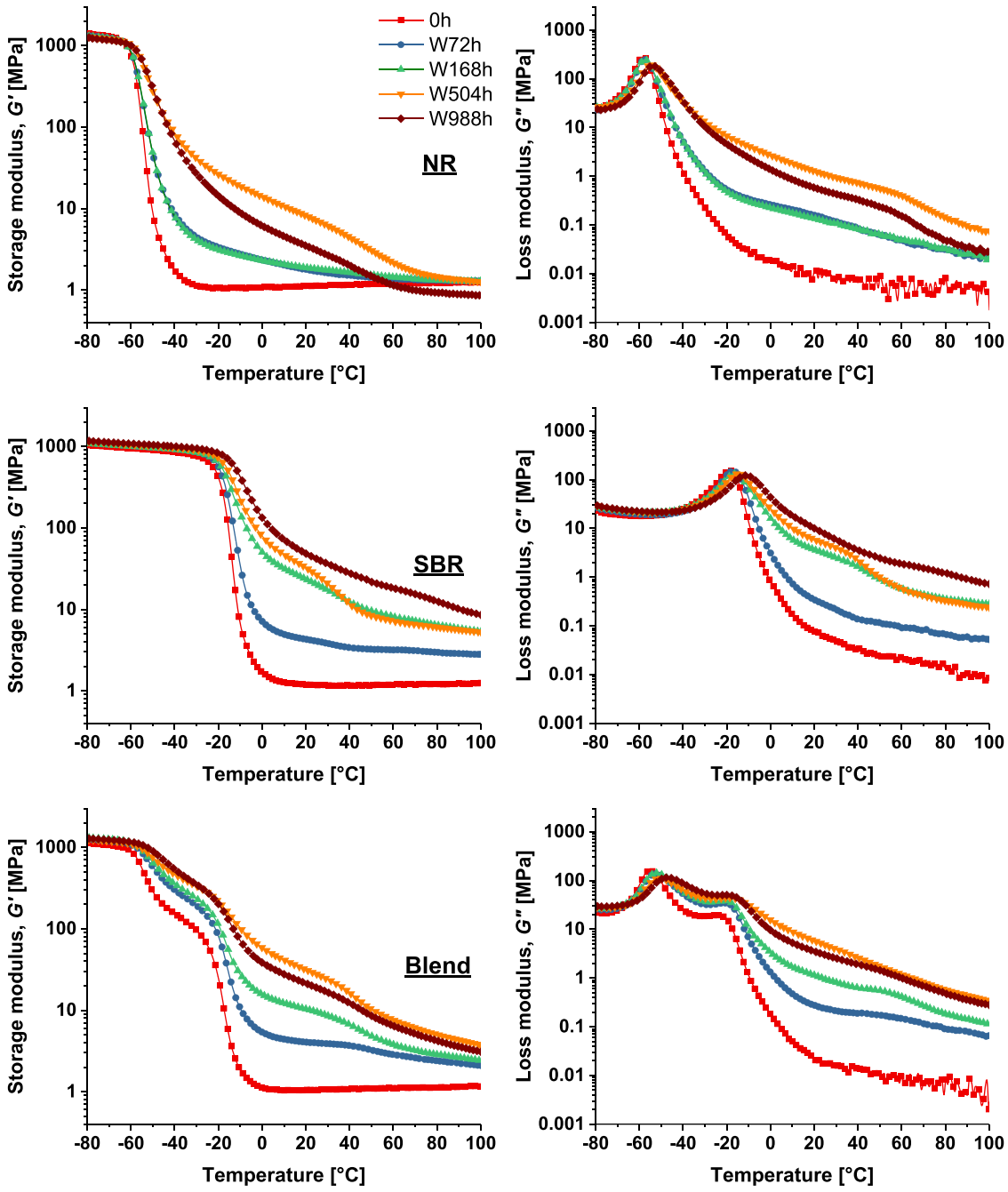

Fig. 2. DMTA temperature ramps of the storage (left) and loss (right) moduli of NR, SBR, and a 50/50 blend of NR and SBR after various weathering (W) durations.

marginal increase in the T_g from the unaged sample is also observable. Distinct changes occur around 500 h of weathering, where stiffening of the sample due to weathering leads to a significant increase in modulus. In addition, a broad second transition around 60 °C can also be seen, which probably is an indication of a second glass transition corresponding to over cross-linked regions of the specimen. With further weathering, stiffness drops below that of the 504 h weathered sample. At higher temperatures, the specimen undergoes softening, well below the plateau modulus of 0 h specimen, due to softening of the hardened regions and the possible presence of decomposed chains.

In the case of SBR, the rubber continuously stiffens in both temperature regions due to weathering-induced hardening. The additional transition appearing upon 500 h of weathering seems to be due to differently aged regions within the sample volume. One may expect that the surface is more aged than the core, thus creating regions of different stiffness [42]. This difference seems to be lost after further weathering. The additional transition observed in the previous weathering interval probably is masked due to the stiffening of the overall sample. The relative stiffening in SBR is higher than NR and remains a decade stiffer even at 100 °C.

The temperature ramps of the blends provide some important insight into the performance of the material in relation to NR and SBR single vulcanizates. Unlike NR, the modulus in the lowest temperature region increases with the weathering duration as observed in SBR. At higher, yet sub-zero temperatures, the 72 and 168 h specimens almost overlap as in the case of NR but diverge somewhat after the SBR T_g. The most significant distinct observation in the blend in comparison to the single vulcanizates is after weathering up to 504 and 988 h. While both NR and SBR respectively demonstrate a decrease and an increase in their moduli beyond their glass transition temperatures at the two weathering

durations, the blend shows almost no deviation in the moduli at these weathering intervals. Fig. S2 in the Supporting Information emphasizes these observations through an overlay of DMTA curves for the three materials at the two weathering durations. A key takeaway message from these arguments is that the cross-link density, which imparts the modulus in the material compositions considered here, is probably identical at the two weathering durations. This aspect will be discussed in detail in Section 4.4.

4.2. Chemical modifications due to weathering as studied by FTIR spectroscopy

Weathering is a depth-dependent phenomenon, where it starts at the exposed surface of the material and then proceeds into the bulk, thus creating a gradient of changes. It is important to note here that the specimen mounting setup in the weatherometer led to one face of the specimen always being hidden from direct irradiation and water sprinkles. One can hence hypothesize that chemical differences between the directly irradiated surface and the other regions, such as the core, would widen with continuous exposure. These chemical modifications are analyzed here by IR spectroscopy.

In a preparatory step, the cross-section of the prepared specimens was first observed in an IR microscope. Pseudo-color Gram-Schmidt plots of IR maps in reflectance mode were generated to provide a visual representation of the chemically modified/unmodified regions within the cross-section of the specimens. The Gram-Schmidt signal provides the integral IR reflectance intensity over all wavenumbers in the spectral range of the experiment. However, it must be considered that the surface quality will also interfere with the scattering intensities.

The warmer colors, i.e., higher Gram-Schmidt signals (higher total integral for all wavenumbers), within the bulk of SBR W168h in Fig. 3 are interpreted as the presence of higher amounts of hydrocarbon structures. In contrast, the cooler colors in the heat map, near the surface (UV irradiated side), are indicative of chemical changes, i.e., modification due to weathering, caused mainly by reaction with oxygen. This also serves as a first proof of the formation of 'skin' and 'core' regions across the sample thickness, due to distinct chemical and, possibly, physical differences. From the microscopic image in the background, a thick skin region for this specimen is observed to be up to about 95 μm from the surface. This demarcation is noted as the moderately modified yellow-green separation line in the Gram-Schmidt plot. Of course, a much more modified, thinner skin can be present immediately at the surface due to the gradient, but analyses of these regions are excluded here. The yellow-green blob on the right-end could be resulting from the topography effects of the surface and highlights the after all qualitative nature of the observation of the skin with this method. Microscopic images of NR weathered up to the same duration demonstrated a skin thickness of about 60 to 80 μm.

The IR microscopy measurements were used as a control to probe the desired regions ('skin' and 'core') through ATR FTIR measurements. Overlays of absorption spectra for NR and SBR weathered to various durations can be found in Fig. 4. A general trend of peak broadening with the weathering duration can be observed in the core-specific spectra of both, NR and SBR.

In both NR and SBR, a broad −OH stretching band is observed between 3660 and 3125 cm^{-1} in the unaged material due to hydroxyl groups present in CBS [2]. The signal intensity increases up to 168 h, possibly due to oxidation or hydration, but reduces thereafter as the additives are consumed [43]. A direct result of weathering in both materials is the occurrence of a carbonyl band at about 1713 cm^{-1} (see * in Fig. 4) after 168 h of weathering and is prominently present in the skin at 504 h but disappears in the core [44].

In NR, the asymmetric =C−H stretching band at 3035 cm^{-1} (i) decreases from 0 h to 504 h [45], while the skin shows its complete loss at 504 h. Likewise, the asymmetric $-CH_3$ stretching (2959 cm^{-1}, ii) and asymmetric $-CH_2-$ stretching (2918 cm^{-1}, iii) bands also reduce with weathering. Further, the symmetric $-CH_3$ stretching and symmetric $-CH_2-$ stretching bands are seen as a single peak at 2849 cm^{-1} (iv) [45], which shows a decrease in intensity and suppression in the skin region at extended weathering.

To put this into context, in a thermo-oxidatively aged NR study [46], the $-CH_2-$ stretching vibration demonstrated peak retention, contrary to the observation made in the present work. Using only UV radiation, dos Santos et al. summarize the formation of different groups in polyisoprene (*cis, trans*, and NR) subjected to various wavelengths [45]. It was concluded that apart from the wavelength, the type of isomer and the pre-condition (presence of groups characteristic of partial oxidation) of the polymer dictate the effects of UV.

The −C=C− stretching vibration occurs at 1662 cm^{-1} (v), whose intensity decreases with weathering. In the fingerprint region, the IR spectra are dominated by $-CH_3$ and $-CH_2-$ bending vibrations at 1452 cm^{-1} (vi) and 1375 cm^{-1} (vii), respectively, and the rocking vibration of $-CH_2-$ at 724 cm^{-1}. As stated before, these peaks also decrease upon increasing the time of weathering, representing a likely explanation for the appearance of the skin in the Gram-Schmidt maps (Fig. 3).

In SBR, the −C=C− stretching of the vinyl group at 1640 cm^{-1} (a) [2] tends to become stronger with successive weathering due to cross-linking. The aromatic −C=C− stretching vibration peak occurs at 1601 cm^{-1} (b) [47] and its contribution is masked by the presence of the −C=C− vinyl stretching. It has been noted that an increase in the intensity of the −COO− stretching vibration at 1541 cm^{-1} (c) in thermo-oxidatively aged SBR is an indication of the carboxylate

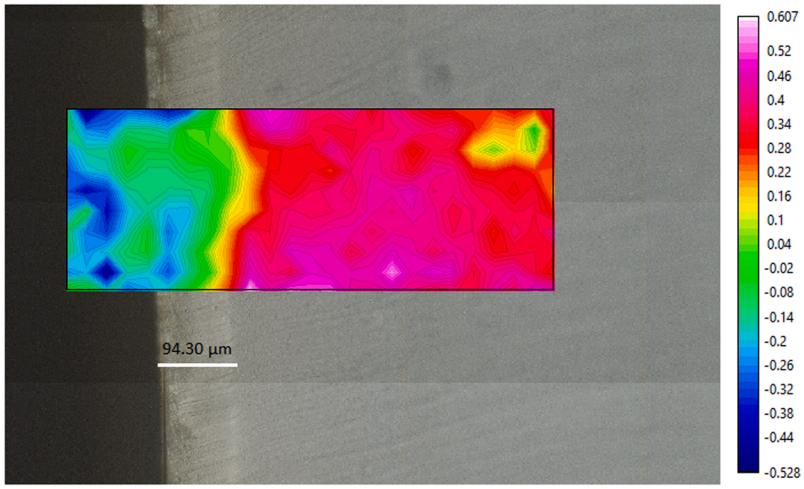

Fig. 3. Gram-Schmidt plot generated using IR microscopy mapping in reflectance mode to assess the chemical modifications across the specimen (SBR W168h) thickness. The blue color end indicates higher weathering-induced modifications, whereas the warmer colors indicate lesser weathering-induced changes. A moderately modified (yellow-green) region is obtained about 95 μm from the sample surface highlighting a distinction between the highly modified 'skin' and the lowly modified 'core'.

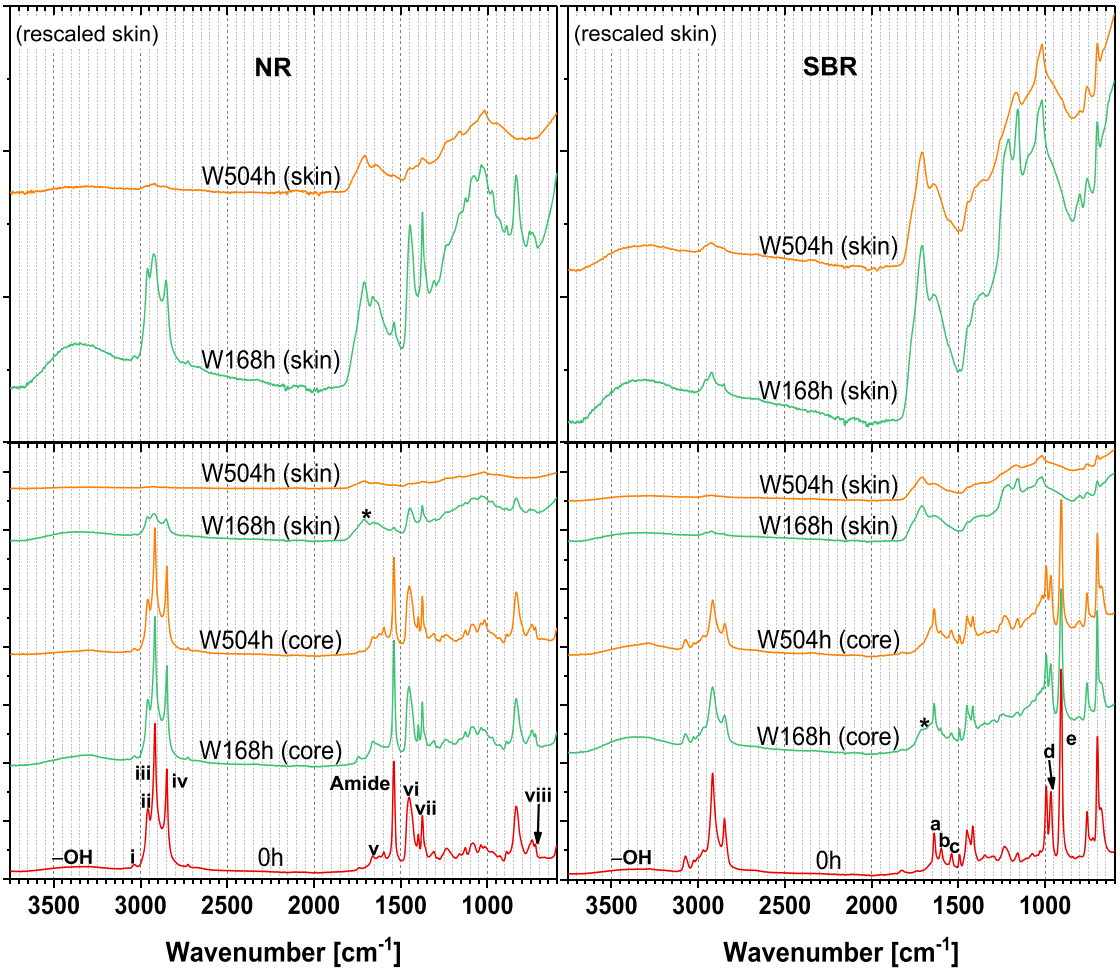

Fig. 4. ATR FTIR absorption spectra for NR (left) and SBR (right) weathered for various durations (bottom boxes). Both the sample series are relatively scaled. The top boxes contain skin-specific spectra rescaled vertically (and equally). The labeled vibration bands are described in the text.

formation as the main product on the material surface [48]. However, such a conclusion cannot be drawn in this study due to the broadening of the −C=C− stretching.

Lastly, the −C=C− vibrations of butadiene at 966 cm^{-1} (d) and 909 cm^{-1} (e) present in the unaged sample disappeared completely after weathering. This is in line with the gas chromatography flame ionization detector (GC/FID) studies on similar samples by Kano *et al.*, which revealed that the relative amount of butadiene with respect to the pristine sample completely disappeared after 100 h of accelerated weathering [44].

From these observations, it can be appreciated that the reactions caused by weathering, mainly involving oxygen, lead to chemical modifications that affect the surface preferentially. Nevertheless, several changes occurring within the core lead to unique physical properties that affect the macroscopic moduli as observed in the previous section.

4.3. Assessment of skin and core regions

4.3.1. AFM nanoindentation measurements

Results from vibrational spectroscopy highlight the formation of chemically different regions upon weathering. One may hence hypothesize that the mechanical properties of these regions would be correspondingly different. To confirm this aspect, AFM nanoindentation experiments were performed at room temperature on SBR W504h, as well as on unexposed SBR (0 h) for comparison. SBR W504h was chosen for its remarkable thermal behavior under dynamic load. The AFM measurements on the skin region of SBR W504h were performed within approximately 30 μm from the directly exposed surface, whereas the measurements on the core region were performed in the central part of the specimen (around 1 mm from the exposed surface). The results are shown in Fig. 5, which displays a plot of cantilever force as a function of indentation depth obtained from the force-distance measurements of the two samples. These indentation curves are indicative of different mechanical properties of the skin and core regions of the weathered SBR.

As can be seen, an increase in applied force causes a larger indentation in the sample. To produce a certain indentation, a significantly different force is needed for all three specimens due to their different mechanical response. Although the correlation between force and indentation depth is nonlinear as described by various nanomechanical models [35,49] and depends on the cantilever's tip radius and shape, the different slopes of indentation curves can be considered to be reflecting the differences in the local stiffness of the material [50,51]. Here, to exclude any effects arising from different tip radii or shapes, and for direct comparison of the data, the same cantilever has been used for the indentation measurements on all three samples. As apparent from Fig. 5, the slope of the indentation curve for the skin region is larger than that for the core region of SBR W504h. This result indicates that the skin region is stiffer compared to the core of weathered SBR. Thus, Fig. 5 clearly illustrates the difference in the stiffness of the two regions of the weathered specimen.

Moreover, the slopes of the curves for the weathered SBR are also remarkably large compared with the unexposed sample. The marked increase in stiffness of the core compared to the unexposed sample indicates a region that has undergone higher cross-linking due to

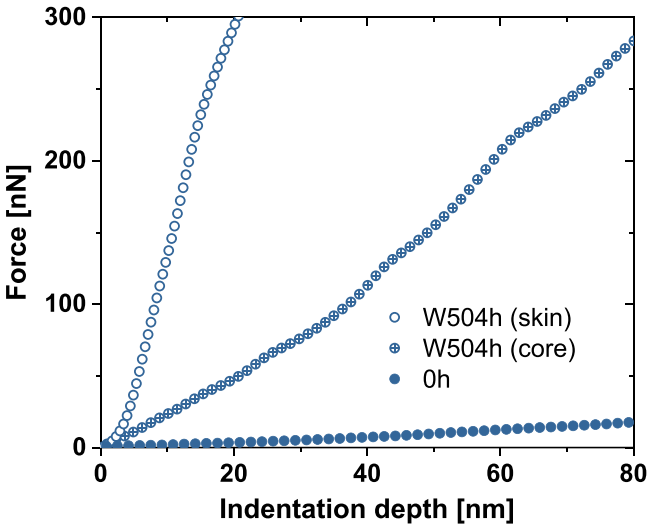

Fig. 5. Representative AFM force vs. indentation depth curves (during approach) for an unexposed (0 h) SBR specimen, and for the 'skin' and 'core' regions of SBR subjected to 504 h of weathering. The skin region is measured within approximately 30 μm from the directly exposed surface. For a direct comparison, all measurements were performed with the same cantilever and experimental parameters.

weathering and corroborates with the shift in T_g observed in the DMTA trends. The second modulus transition observed in the DMTA plot of SBR W504h is, thus, resulting from the even stiffer skin region, as confirmed here by AFM. As such, from the AFM results and the concepts of diffusion of oxygen [42,52], it can be concluded that the moduli of the samples presented in Fig. 2 are, in fact, an outcome of a *gradient* of depth-specific moduli.

From a physical point of view, due to the intermittent water sprays, associated expansion and shrinkage of the sample may occur due to the associated temperature changes. These effects in the core region will be somewhat reduced and delayed. Eventually, this results in the formation of distinct stiff skin and soft core that develop different linear coefficients of expansion. For up to 100 h of weathering of SBR Kano, *et al.* observed a 0.5 % volume change due to temperature increase during photo irradiation and temperature decrease during water sprays [44]. This periodic thermal treatment leads to differential expansion and contraction of the skin and the core. In the present study, the long-term weathering of SBR for 504 and 988 h caused a visual caving-in of the specimen towards the irradiated surface due to contraction and stretching of the rear surface due to expansion. Naturally, the clamped ends did not demonstrate this deformation, leaving the unclamped region to appear like a shallow boat.

As another consequence, successive heating/cooling has been observed to cause crazing (or elephant skin formation) on the sample surface, which also propagate to the depth of the specimen. Although these small unoriented connected cracks are typical of an unstressed vulcanizate, the difference in shrinkage leads to the build-up of stresses and the development and propagation of microcracks. The possibility of surface erosion due to spraying cycles cannot be ruled out.

Understandably, this phenomenon would be amplified when weathering up to 988 h as in the case of the present study. These cracks act as a pathway to the leaching of water and more chemical attacks into the bulk of the specimen [34]. The intensity of cracks in SBR is aligned with its poor resistance to crack growth despite having a strong resistance to crack formation. In the case of NR, cracks are formed relatively quickly but grow rather slowly [53]. This can be confirmed from the seemingly protected core of NR vulcanizates as seen in FTIR results.

From these collective arguments it may perhaps be hypothesized that once the integrity of the stiff skin is destroyed, such as by a pre-stretching to a moderately larger strain, the G' of SBR associated with the skin (in Fig. 2) will be effectively reduced. Thus, an 'as-is' interpretation of bulk mechanical results is difficult if not impossible in such materials. More detailed mechanical experiments along these lines were unfortunately beyond our present scope.

4.3.2. *Quantification of skin and core regions by T_2 analyzes*

As introduced in Section 3.1, the different fractions in a rubber vulcanizate (detected in terms of their proton fractions) can be distinguished based on their respective T_2 times, which makes quantifying the skin and core regions possible. To emphasize the effects of the stiff skin and the soft core, the hardened surface of the 504 h weathered SBR was shaved off using a blade to a depth of roughly 200 μm for separate measurements.

Firstly, the results of a three-component modified exponential decay fit to NR and SBR vulcanizates at different weathering durations are partially presented in Fig. 6A. To recall, the rigid-limit coupling corresponds to a $T^{eff}_{2,r}$ of about 20 μs, which can be assigned to the highly constrained fraction. With a shape parameter (β_r) fixed to 2, the amount of this rigid fraction (f_r) was almost negligible in SBR and about 1.5 % in NR at 0 h. The latter is likely associated with the presence of proteins.

As is shown in Fig. 6A, with weathering the rigid fraction in NR increases, the addition being the oxidized surface, which stabilizes at about 4 % between 504 and 988 h. On the contrary, in SBR, a continuous increase in rigid fraction up to about 7 % occurs due to oxidation of the surface and the underlying layers. The larger amount of rigid components in SBR compared to NR corroborates with the observation made by DMTA towards high temperatures.

The second fitting fraction, regarded as the mobile 1 fraction (f_{m1}) (not shown in Figure) with apparent transverse relaxation time $T^{eff}_{2,m1}$ (Fig. 6A), corresponds to the component that mainly represents the cross-linked bulk. The third fraction composed of defects is represented as the mobile 2 fraction (f_{m2}). These two fractions can be better characterized by MQ measurements and hence, are deferred to Section 4.4.1. Nevertheless, for completeness, the fitting yielded a negligible amount of defect fraction in all SBR samples. NR weathered up to 988 h contained up to about 9 % defects with a $T^{eff}_{2,m2}$ of about 12 ms. The corresponding shape parameter β_{m2} was force-fitted to a limiting minimum value of 0.8 (stretched exponential), meaning that the mobile 1 and 2 fractions cannot be reliably separated in all cases. $T^{eff}_{2,m1}$ (also, in Fig. 6A) corresponding to the majority bulk remains relatively unchanged in NR, whereas a gradual decrease is observed in SBR due to an increase in cross-link density with the weathering duration. An increasing f_r and decreasing $T^{eff}_{2,m1}$ in SBR suggests the presence of a gradient of stiffness due to weathering. In NR, the skin and core could be somewhat distinct. These aspects would become clearer when discussing the cross-link densities in Section 4.4.

For the depth-specific studies, the separated skin and core of 504 h weathered SBR were compared with an intact sample. As an illustration, MSE-FIDs (only) for the two regions and an intact SBR weathered up to 504 h are shown in Fig. 6B. A two-component fitting yielded about 8 % rigid fraction for the skin sample, and as expected, 0 % for the core sample. The second fitting component produced a T^{eff}_2 of 45 μs and 80 μs, respectively, thus emphasizing gradient stiffening below a relatively hard surface in SBR.

4.4. *Changes in network density by weathering*

4.4.1. *Low-resolution NMR studies*

The efficiency of cross-linking, apart from the choice of cross-linker system and the processing conditions, is governed mainly by the extent of unsaturation present in the polymer chain. The higher unsaturation in NR provides a potential for a higher number of cross-links. It also aids in faster cross-link formation, which is confirmed by the shorter curing

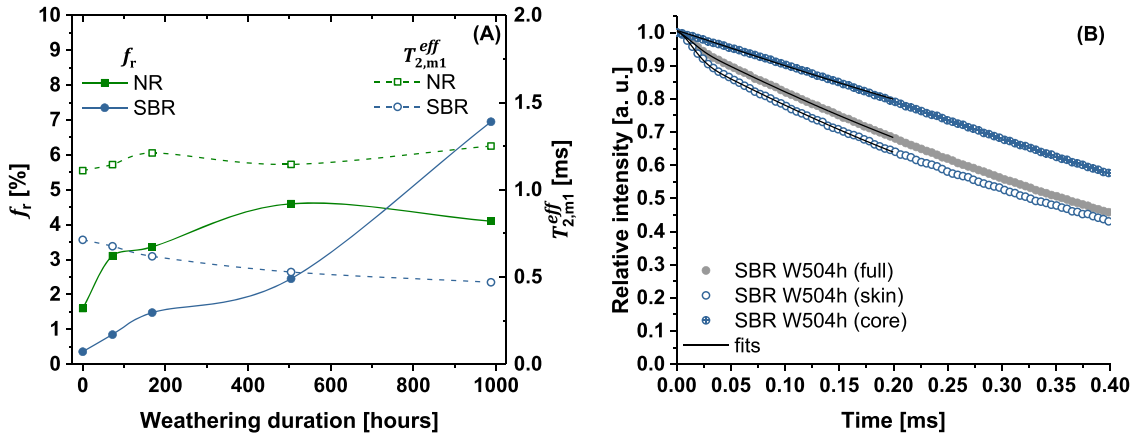

Fig. 6. (A) The variation of weathering-induced rigid fractions (f_r) that correspond to a transverse relaxation time of 20 μs for NR and SBR at different weathering intervals. The right *y*-scale shows relaxation times of a comparatively slowly decaying softer, mobile majority fraction (f_{m1}). See Section 4.4.1 for a discussion of a much more slowly decaying defect fraction. (B) MSE-FID decays of the skin and core regions of the SBR W504h specimen obtained after crudely slicing the exposed layer (thickness of roughly 200 μm). MSE-FID of an intact sample is plotted for reference.

time. The effect of sulfur cross-linking in NR and SBR, in addition to the effect of entanglements, can be ascertained from the values of D_{res} in Fig. 7A corresponding to 0 h. Interestingly, due to differences in the density of unsaturation between them, NR and SBR, upon vulcanization, produce identical D_{res} despite their largely different starting values of about 70 Hz and 135 Hz, respectively in the uncross-linked (pristine) state (not shown in Figure). This is for sure coincidental, as both M_e (entanglement molecular weight) and the reference coupling of the monomer units (D_{ref} in Eq. (1)) are different. The distribution widths of these samples are also similar to the values before cross-linking. Thus, it can be deduced that sulfur does not affect the inherent distribution of these constraints within the sample volume, or sulfur characteristically leads to a narrow distribution of cross-links. Analogous to the single vulcanizates, the 50/50 blend also cross-links to a similar extent. The experimentally measured coupling width is also identical to the weighted average of σ_{ln} of the two constituent vulcanizates, thus indicating that sulfur distributes itself non-preferentially within the phases of the blend.

Distinct variations occur in the samples when exposed to the aging elements in the weatherometer as seen from the evolution of cross-link density in Fig. 7A. The biggest change can be seen in SBR, where degradation generally occurs through cyclic cross-linking, which leads to an increase in stiffness (embrittlement). The corresponding coupling distribution width compliments the formation of different chain lengths between cross-links.

As established earlier, the regions closer to the surface undergo stiffening due to direct exposure to irradiation, oxygen, water, and heat. Like in the T_2 measurements, the constrained fractions also show up in the I_{nDQ} signal. This can be seen as a step-up in the I_{nDQ} curve at the short evolution times of up to 100 μs (probing lower values is not feasible due to the pulse sequence length). The build-up curve in Fig. 7B represents this feature for SBR weathered up to 504 h.

A modified bimodal fitting function [17] can be used to separately fit these hardened surface fractions and those that lie beneath that are comparatively less aged. The input parameters to the fitting function are a fixed coupling value $D_{med,2}/2\pi = 12$ kHz, and distribution value $\sigma_{ln,2} = 0.01$, where 12 kHz is sufficiently high to have a constant intensity contribution in the plateau region of the respective build-up curve. The constrained fraction is around 2.5 %, which is lower than the actual value because the pulse sequence is inefficient for these components.

The other mode ($D_{med,1}$), represented in Fig. 7A is obtained as a fitting result to the data points of the build-up curve *after* those that correspond to the highly cross-linked regions (step-up), and thus represent the bulk of the sample. In SBR, prolonged exposure leads to further stiffening with a net $D_{med,1}$ gain of about 33 %. Likewise, $\sigma_{ln,1}$ shows an increase in the coupling distribution due to chain modifications.

Interestingly, this increase in cross-link density of SBR is rather marginal compared to the (approximately) 15-fold increase in the slope of the core region of SBR W504h with respect to the unexposed sample, as observed from AFM. This can be explained by the temperature-dependent gain in modulus of aged SBR with respect to that of unaged SBR. The gain in G' for the 504 h aged SBR is higher at 25 °C (23-fold) than at 80 °C (5-fold), the two temperatures being the measurement temperatures for AFM and NMR, respectively. This is, of course, without denying that the modulus in DMTA is a combined effect of, both, the skin and core regions. Another factor for the observed (apparent) inconsistency in property change is a systematic error originating from the choice of the cantilever in the AFM experiment. The cantilever used in the AFM experiments was chosen in accordance with the stiffness of SBR weathered for 504 h. The same cantilever was used to probe the rather soft unaged SBR, which could have led to penetration of the cantilever tip into the specimen.

In the case of NR, contrary to SBR, the D_{res} appears to remain unchanged upon weathering up to 168 h. However, the broadening of coupling distribution suggests the modification of covalent bonds. The conventional sulfur-vulcanization system is known to majorly produce polysulfidic bonds [54]. The broadening of coupling distribution is thus suggestive of the reformation of polysulfidic bonds into shorter variants like the mono- and disulfidic bonds [55]. The same observation has been made earlier with NR exposed to thermo-oxidative aging at 80 °C [17]. Oxidation-induced chain scission is another contributing factor to the broadening of the coupling distribution. Upon continued weathering, the bulk of NR undergoes a reduction in cross-link density due to the extensive decomposition of main chains. These changes are also evident in the distribution width.

In the blend, until 168 h, D_{res} varies only moderately and produces values that are similar to those of NR. The corresponding changes in $\sigma_{ln,1}$, however, suggest distinct chemical changes within the sample volume which are again indicative of the maturation of sulfur bonds as seen in NR. A standout observation here is that the blend ages less in comparison to its expected value (wtd. blend), plotted for reference. This is a numerically measured weighted average of NR and SBR single vulcanizates. By acknowledging the similarity in D_{res} of NR and the blend up to 168 h, one can infer that the bulk of the SBR phase experiences lesser chemical changes in the blend than when it is a pure vulcanizate.

At the extended weathering durations, the coupling strengths of the

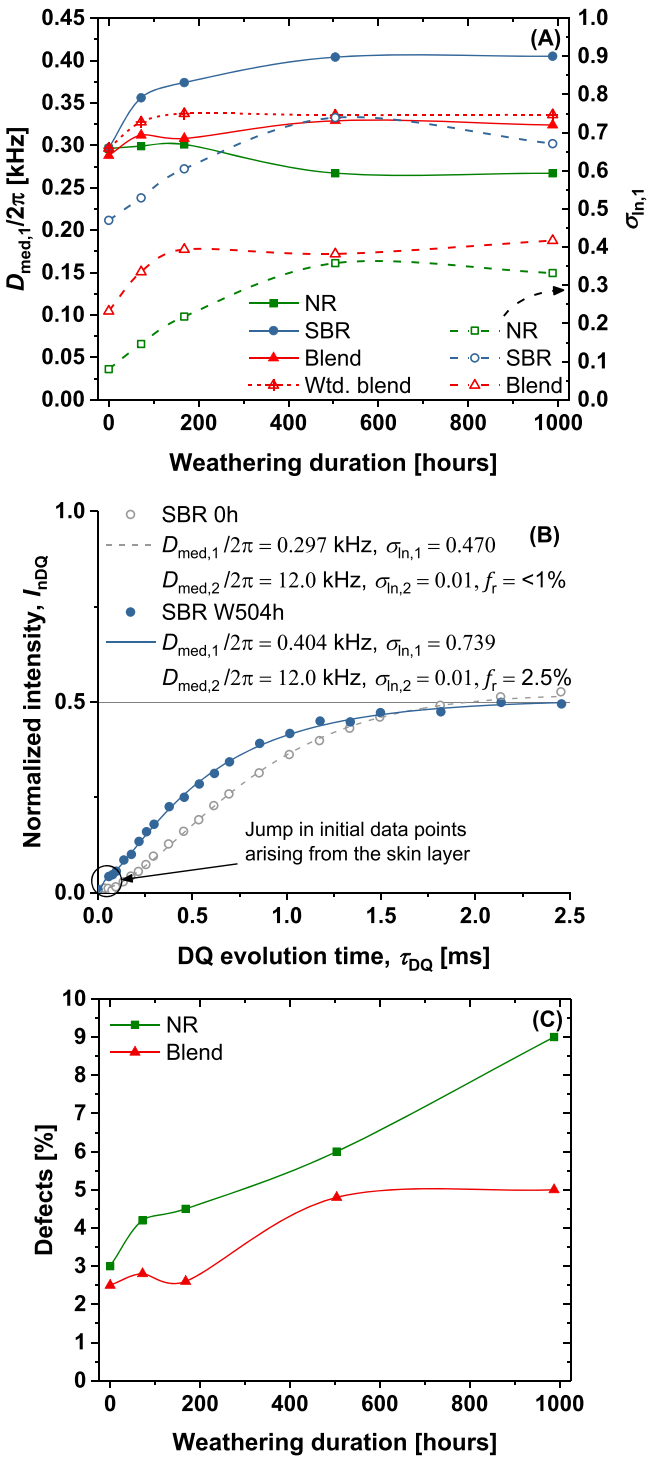

Fig. 7. Results of MQ NMR measurements for NR, SBR, and their 50/50 blend. (A) Cross-link densities (solid lines) and their distributions (dashed lines) within the polymer bulk. The weighted (wtd.) average of D_{med} for the blend (short-dashed line), based on the D_{med} of NR and SBR, is shown for comparison (see text). An additional fitting mode was used to account for surface-stiffening observed in the samples due to weathering based on the rigid fractions in Fig. 6A. (B) Demonstration of the rigid fraction as a step-up in the I_{nDQ} signal at shorter DQ evolution times for SBR W504h. Its coupling is set to a fit-adequate value of 12 kHz (see discussion). (C) The defect fraction obtained from normalization. No defects are detected in SBR.

blend are intermediate to those of NR and SBR. Interestingly, no significant variation of $D_{med,1}$ can be observed for the three materials between 504 and 988 h. Also, the invariance of the corresponding coupling widths suggests no significant chemical modifications in the samples beyond 500 h. In comparison to the previous work [17], these trends highlight that sulfur-cross-linked NR is chemically unstable at higher temperatures (thermo-oxidative aging at 80 °C), whereas sulfur-cross-linked SBR is more susceptible to artificial weathering.

The defect fraction (in Fig. 7C) obtained by an exponential decay fit to $I_{\Sigma MQ}$ during normalization is analogous to the third fraction obtained through T_2 analyses in Section 4.3.2. The amount of defect fraction in NR, corresponding to a T_2 relaxation time of about 15 ms, changed from about 3 % for the unaged sample to 9 % for the most weathered sample. In the case of SBR, as expected, no presence of defects was detected. This confirms the complete cross-linking in SBR due to weathering. For the blend, surprisingly, the amount of defect fraction varied from about 2.5 % to only 5 %. Assuming that the defect amount of the SBR phase remains negligible also in the blend, the lower amount of overall defects in the blend is an unexpected finding and probably suggests that NR is also protected from weathering when it is a part of the blend.

More coupling information can be obtained by Fast-Tikhonov regularization (*ftikreg*) of the normalized build-up data [41]. This procedure yields a visual representation of the distribution of D_{res} within the samples (Fig. 8). The median value of D_{res} (D_{med}) corresponds to the value at which the normalized integral of these curves is 0.5. The inherent (in)homogeneity of spins in uncross-linked (pristine) NR and SBR remains relatively unchanged upon vulcanization (0 h) but increases due to weathering. Already upon 72 h of weathering of SBR, the formation of a small amount of rigid fraction can be observed towards the higher coupling end of the distribution. In addition to this, SBR at 504 and 988 h of weathering contains small amounts of cross-linking-induced, newly formed constrained fractions that are ubiquitous in the coupling distribution graphs. In the case of the blend, proportional changes can be observed.

To summarize the low-field results, SBR undergoes perfectioning of cross-links leading to stiffening, whereas NR demonstrates both cross-linking and chain scission that lead to stiffening and softening processes, with chain scission eventually dominating. Interestingly, measurements of the blend material reveal that the NR and SBR phases are protected when they are a part of the blend in contrast to the respective single vulcanizates.

4.4.2. *Phase-resolved studies of the evolution of cross-link densities*

MAS NMR experiments benefit from the resolution of a spectrum into defined peaks. This enables phase-specific studies in polymer mixtures. With every integer rotor period and a rotor frequency of 10 kHz, the shortest DQ evolution time achievable in the current setup is 100 μs. Hence, the DQ signals obtained here are free of contributions from the rigid fractions.

The three proton resonances in NR corresponding to CH, CH_2, and CH_3, as has been previously demonstrated [31], and adapted in Table 1 yield identical coupling, and the spectral average is similar in magnitude to the low-field experiment value.

Unexposed SBR yields a spectral average coupling value of about 0.280 kHz. The lowest value is attributed to the phenyl ring due to its motional freedom about the main-chain CH bond. The highest coupling corresponds to the groups at chemical shifts of 1.9 ppm and 1.2–1.8 ppm, coming majorly from the main chain protons of vinyl polybutadiene. This copolymer is also responsible for the spin heterogeneity in the SBR grade considered in this study.

The changes occurring in the samples due to weathering are represented as a ratio of coupling constants and their distribution after 504 and 988 h of weathering to their corresponding values at 0 h in Fig. 9. The chemical groups have been arranged from left to right in the sequence of resonances as NR-only → mixed → SBR-only. In the case of NR (Fig. 9B), one can observe that the polymer cross-link density

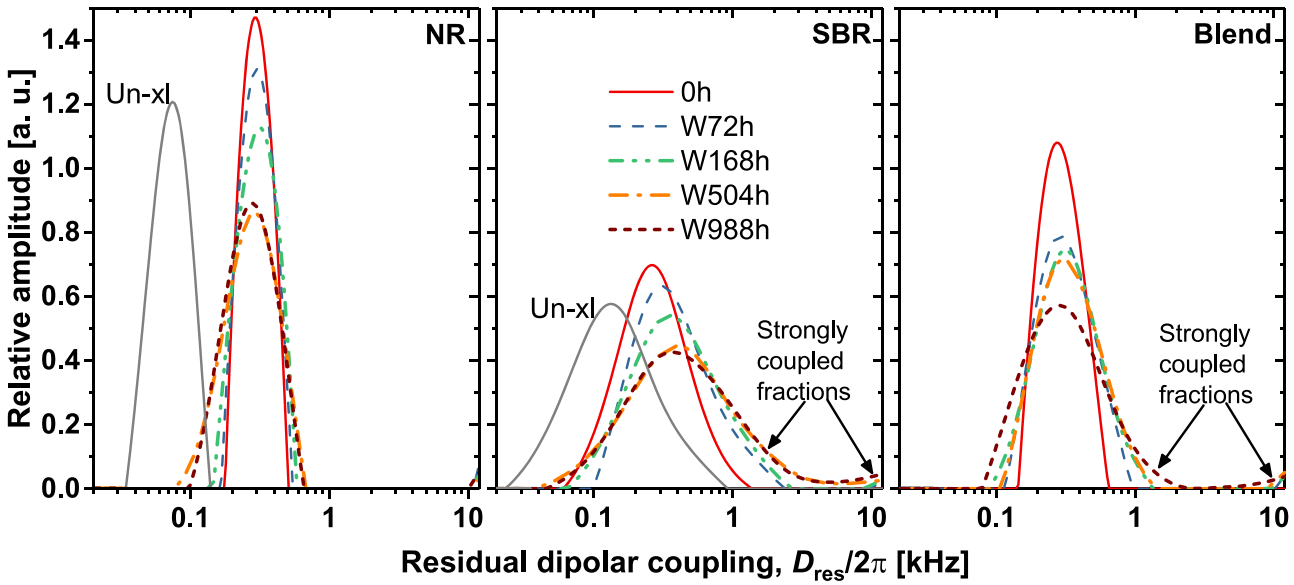

Fig. 8. Changes in the distribution of cross-links due to weathering. These are obtained by regularization of the normalized DQ data. The presence of strongly coupled fractions can be seen in SBR and the blend. The inherent coupling distributions of uncross-linked (Un-xl) NR and SBR are plotted for reference.

Table 1
Phase-resolved D_{med} and respective σ_{ln} for the unexposed materials. (Adapted from Ref. [17]).

Chemical group/s	Chemical shift, δ [ppm]	NR		SBR		Blend	
		$D_{med,2}/2\pi$ [kHz]	σ_{ln}	$D_{med,2}/2\pi$ [kHz]	σ_{ln}	$D_{med,2}/2\pi$ [kHz]	σ_{ln}
$C_6H_5^{PS}$	7.2 – 7.7	–	–	0.233	0.278	0.200	0.236
$CH^{1,4}$, $CH^{1,2}$ *(vinyl)*	5.5 – 6.1	–	–	0.258	0.352	0.232	0.323
CH^{NR}	5.5	0.287	<0.01	–	–	0.291	0.038
$CH_2^{1,2}$ *(vinyl)*	5.3	–	–	0.284	0.337	0.256	0.316
CH_2^{NR}, CH^{PS}, $CH_2^{1,4}$	2.1 – 2.8	0.293	0.044	0.292	0.420	0.287	0.215
CH_3^{NR}, $CH^{1,2}$	1.9	0.278	0.112	0.315	0.449	0.281	0.200
CH_2^{PS}, $CH_2^{1,2}$	1.2 – 1.8	–	–	0.313	0.518	0.282	0.669
Spectral average	–	0.287	0.104	0.278	0.455	0.274	0.303

reduces after weathering to 504 h, and is analogous to the observations made using the low-field experiment. The increase in its coupling width is an indication of the increasing cross-linking inhomogeneity. This aspect is pronounced in the CH and CH_2 moieties, as these sites are directly affected by the various reactions (S-modification, chain scission, cross-linking, etc.) occurring in the vicinity. Here it is important to note that despite the observed widening, the average absolute value of σ_{ln} after 504 h of weathering is about 0.410.

Weathering SBR to 504 h leads to an average increase of about 35 % in D_{med} across all chemical environments of the rubber (Fig. 9C) and complements the results of the low-field. Unlike in NR, the change in coupling distribution width is almost identical for all the proton environments.

Upon 988 h of weathering, NR undergoes a further reduction in its cross-link density. This finding is different from the low-field measurement where the D_{med} seemed to have stabilized at extended exposure durations. The corresponding distribution appears to have slightly narrowed down upon extended weathering. This is consistent with the low-field results and could be due to the recross-linking of some weakly coupled segments that are present after 504 h of weathering, thus leading to uniformity of chain lengths between cross-links.

Perhaps the most important observation in NR from the high-field and low-field measurements is that as the surface stiffens, the core softens. This behavior suggests that the hardened surface acts as a barrier to layers underneath wherein chain scission dominates.

With SBR, weathering to 988 h shows a reversal of the cross-linking trend. The average coupling strength reduced from 0.377 kHz (after 504 h) by about 50 to 0.326 kHz (after 988 h). This is a rather surprising finding that was not observed in the low-field experiment. Variations can be observed at resonances ii, iii, and vii (see Fig. 9C), which correspond to the main chain protons of the three monomers in SBR, suggesting changes in the bonding situation in due to weathering. But the cross-link distribution remains almost unaffected by weathering.

NR and SBR have similar solubility parameters of about 16.7 $MPa^{1/2}$ and 17.5 $MPa^{1/2}$, respectively [56], making their blends technologically relevant due to macroscopic miscibility as a result of low interfacial tension. Nevertheless, they tend to exhibit phase separation on a microscopic scale due to their molecular incompatibility and thus provide scope for potential variations in the blend phases. The low-field measurements discussed earlier suggest that NR and SBR cross-link to similar extents in the blend, as do their corresponding single vulcanizates. However, MAS experiments reveal some inconsistencies in SBR. The SBR phase cross-links to a lesser extent in the blend compared to its single vulcanizate. This is despite its preferential and faster reaction rate with CBS accelerator than that of NR [17,57]. Thus, a relatively softer SBR phase is present in relation to an NR phase which yields identical D_{res} as its single vulcanizate.

The changes arising in the blend upon weathering are evident in Fig. 9A. Upon 504 h of weathering, the extent of changes in the NR-containing resonances is minimal, especially the D_{res} of CH resonance appears unchanged, albeit with a small broadening of the coupling constant. On the other hand, a distinct increase in D_{res} can be observed for the pure SBR resonances. The corresponding coupling distribution widths across the various resonances are largely similar to those obtained from the single vulcanizates. Despite the finite increase, the increase in D_{res} of SBR-phase resonances is, on average, still lower than the

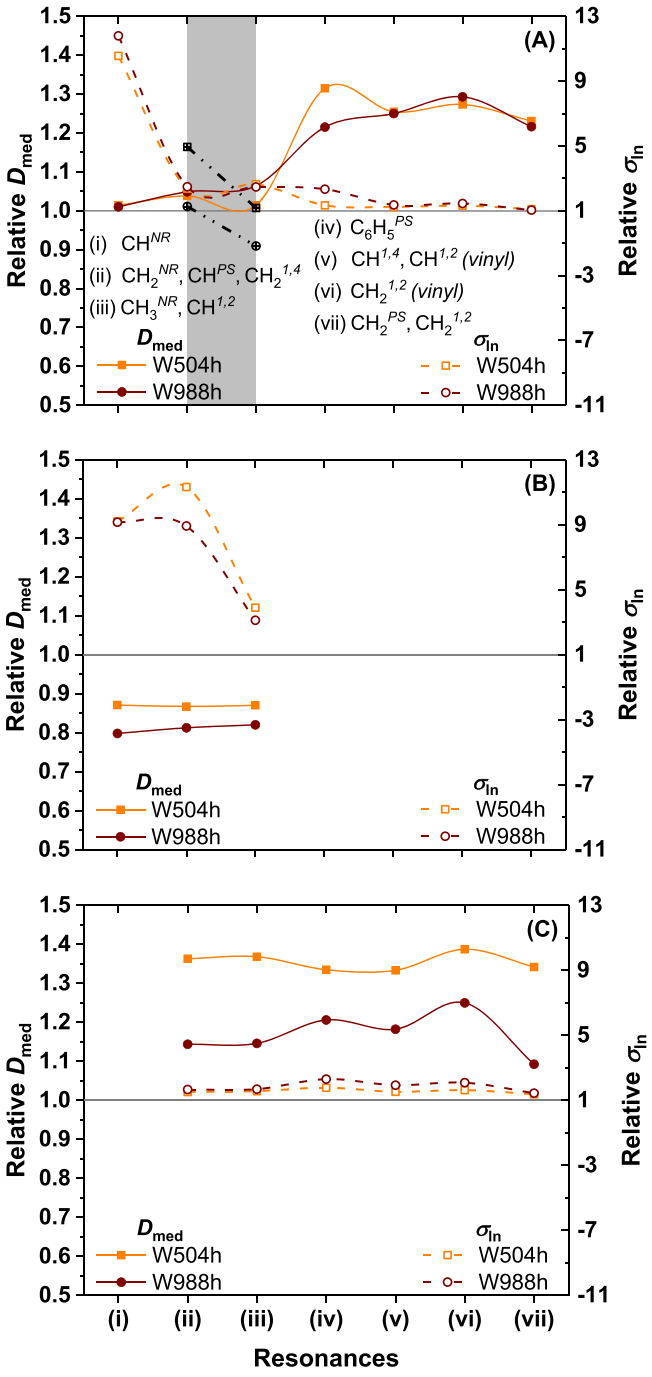

Fig. 9. Relative changes in cross-link densities and their distribution described as a ratio of coupling parameters at 504 and 988 h weathering to those at 0 h for (A) blend, (B) NR, and (C) SBR. "Vinyl" in parentheses refers to the vinyl part of 1,2-polybutadiene. The lines are a guide to the eye only. The gray shaded area in (A) highlights the overlapped resonances in the blend. The crossed open symbols (square: 504 h, circle: 988 h) represent the proton-weighted averages of D_{med} of the mixed resonances obtained from the correspondingly weathered single vulcanizates and thus highlight the "protective" nature of the blend.

single vulcanizate. This is probably due to a lowly cross-linked SBR phase before weathering.

Upon further weathering to 988 h, the distribution of cross-links in both phases almost overlaps with the values obtained after 504 h, thus suggesting that the chain lengths remain virtually unaffected. This is confirmed by the comparably similar changes in D_{res} even after almost doubling the weathering duration and explains the reason for the almost-identical moduli of the blend at the two durations. This is a rather astonishing behavior of the blend compared to the single vulcanizates, where NR underwent continuous softening over the two weathering intervals, and SBR demonstrated a stiffening and then softening property at 504 and 988 h, respectively.

To emphasize this experimental finding, Fig. 9A also compares the 'expected' values of changes in D_{res} of the blend based on proton-weighted averages from the single vulcanizates at the two intervals for the mixed resonances (gray shaded area) at resonance locations ii and iii (see Fig. 9A). Thus, this highlights the effects of softening and stiffening that should have been observed in the blend but are rather weak. These observations made through MAS also corroborate with the lower defect fraction in the blend observed through the low-resolution experiment. These arguments collectively demonstrate that the two polymers are protected in the blend even at prolonged weathering durations. In other words, under the experimental conditions discussed here, the blend lasts longer and is hence technologically better suitable than the constituent single vulcanizates.

5. Conclusion

In this study, the molecular and bulk changes in sulfur-cross-linked NR, SBR, and their blend (50/50 ratio by phr) subjected to artificial weathering were monitored by various techniques. At longer weathering durations, DMTA measurements revealed stiffening in NR that softened almost entirely at higher temperatures. The stiffening was pronounced in SBR. This contributed to an additional softening transition which showed significant modulus even at 100 °C. The chemical origins of these were evaluated by FTIR, which revealed modification of the surface layer into a stiff skin due to oxidation processes aided by various weathering parameters. The regions below this skin layer oxidized to a lesser extent due to the barrier-like behavior of the skin. AFM nano-indentation measurements at various depths of SBR weathered up to 504 h confirmed the oxidation-induced stiffening that imparted an additional transition in DMTA experiments.

Further analyses of the skin and core by NMR T_2 studies suggested a continuous increase in the skin fractions in SBR up to about 7 % for 988 h of weathering. In NR, the stiff fraction stabilized between 504 and 988 h at about 4 %. It was also indicated that the bulk of NR probably remained unchanged due to prolonged weathering, whereas in SBR a gradient of stiffness existed beneath the stiff skin due to continuous cross-linking.

The cross-link density measurements by an MQ pulse sequence on a low-field spectrometer highlighted an increase in the cross-linked density of SBR up to 504 h by 33 %, which remained unchanged up to 988 h. In contrast, NR had the same cross-link density up to 168 h, which then dropped by 10 % approaching 504 h. The stagnation in cross-link density up to 168 h was attributed to a modification of polysulfidic bonds to the lower, disulfidic and monosulfidic variants and due to oxidation-induced chain scission.

In the blend, cross-link density varied only moderately, which was lower than a calculated average obtained by weighting D_{res} of NR and SBR single vulcanizates, thus showing that blends age lesser compared to their single vulcanizates. The cross-link distribution values indicated the formation of different chain lengths between cross-links due to weathering in all samples. Further, it was observed that weathering caused the formation of defects in NR and the blend but was non-existent in SBR due to complete cross-linking. Thus, the MQ experiments prove the existence of a stiff skin but a soft core, where chain scission reactions dominate. In SBR, a stiff skin is obtained with a core that is still generally harder than the unaged sample.

Phase-resolved studies by ^{1}H DQ MAS NMR provided some additional insights into the weathered samples. In NR, unlike the low-field measurements, the cross-link density reduced continuously between 504 and 988 h. In the case of SBR, the cross-link density increased up to 504 h but then reduced after extended weathering with no change in the

distribution of cross-links. The most fascinating outcome of the high-field experiments was the formation of a distribution of cross-links in the blend phases, where a soft NR phase varied insignificantly in its cross-link density for the entire weathering duration. A strongly cross-linked hard SBR phase remained invariant to weathering between 504 and 988 h. These observations are supported by the similarity in the dynamic moduli of the blend at the two durations. Via the inherent proton counting feature of NMR, it was established that the blend was relatively resistant to weathering compared to its single vulcanizates, thus making the blend an ideal choice for long-term applications.

CRediT authorship contribution statement

Akshay Karekar: Conceptualization, Methodology, Validation, Formal analysis, Investigation, Data curation, Writing – original draft, Visualization, Project administration. **Carsten Schicktanz:** Investigation, Visualization. **Muhammad Tariq:** Investigation, Writing – original draft, Visualization. **Katja Oßwald:** Conceptualization, Methodology, Validation, Resources, Supervision. **Katrin Reincke:** Conceptualization, Methodology, Validation, Resources, Writing – review & editing, Supervision. **Valentin Cepus:** Validation, Investigation, Resources, Writing – original draft, Writing – review & editing, Visualization. **Beate Langer:** Resources, Writing – review & editing, Supervision, Funding acquisition. **Kay Saalwächter:** Conceptualization, Methodology, Software, Validation, Resources, Writing – review & editing, Supervision, Project administration, Funding acquisition.

Declaration of Competing Interest

The authors declare that they have no known competing financial interests or personal relationships that could have appeared to influence the work reported in this paper.

Data availability

Data will be made available on request.

Acknowledgments

The authors thank the Land Sachsen-Anhalt and the European Social Fund (ESF) [grant number ZS/2016/08/80644]. M.T. acknowledges funding from the Deutsche Forschungsgemeinschaft (DFG, German Research Foundation)—Project-ID 189853844—TRR 102. M.T. also thanks Mr. Qiang Yu for assistance in microtomy. A.K. thanks Dr. Marcus Schoßig at Polymer Service GmbH Merseburg for facilitating weathering of the specimens, and Prof. Thomas Thurn-Albrecht for access to ARES G2 and his insights on AFM.

Supplementary materials

Supplementary material associated with this article can be found, in the online version, at doi:10.1016/j.polymdegradstab.2023.110267.

References

[1] J.E. Pickett, Introduction to polymer weathering, stabilization, and testing. Service Life Prediction of Polymers and Coatings, Elsevier, 2020, pp. 1–18, https://doi.org/10.1016/b978-0-12-818367-0.00001-1.
[2] N. Rezig, T. Bellahcene, M. Aberkane, N. Abdelaziz, M. Thermo-Oxidative, Ageing of a SBR rubber: effects on mechanical and chemical properties, J. Polym. Res. 27 (11) (2020) 1–13, https://doi.org/10.1007/S10965-020-02330-Y.
[3] J.E. Pickett, D.A. Gibson, S.T. Rice, M.M. Gardner, Effects of temperature on the weathering of engineering thermoplastics, Polym. Degrad. Stab. 93 (3) (2008) 684–691, https://doi.org/10.1016/J.POLYMDEGRADSTAB.2007.12.013.
[4] Tinker, A. J. A.J. Tinker, K.P. Jones, Introduction — the book and rubber blends. Blends of Natural Rubber, Springer, Dordrecht, 1998, https://doi.org/10.1007/978-94-011-4922-8. Tinker, A. J.
[5] C.M. Roland, A.K. Bhowmick, H.L. Stephens, Rubber-rubber blends: part I. Handbook of Elastomers, Marcel Dekker, New York, 2001, pp. 197–225.
[6] A.V. Chapman, A.J. Tinker, Vulcanization of blends – crosslink distribution and its effect on properties, Kautsch. Gummi Kunstst. 56 (10) (2003) 533–544.
[7] C.M. Roland Immiscible rubber blends. In advances in elastomers I, P.M. Visakh, S. Thomas, A.K. Chandra, A.P. Mathew, eds., Advanced Structured Materials, Springer Berlin Heidelberg: Berlin, Heidelberg, 2013, Vol. 11. 10.1007/978-3-642-20925-3.
[8] S. Schlögl, M.L. Trutschel, W. Chassé, G. Riess, K. Saalwächter, Entanglement effects in elastomers: macroscopic vs microscopic properties, Macromolecules 47 (9) (2014) 2759–2773, https://doi.org/10.1021/MA4026064.
[9] A.I. Dzulkifli, C.M.S. Said, C.C. Han, Determination of crosslink concentration by mooney-rivlin equation for vulcanized NR/SBR blend and its influence on mechanical properties, Malays. J. Anal. Sci. 19 (6) (2015) 1309–1317.
[10] R. Srithawatpong, Z.L. Peng, B.G. Olson, A.M. Jamieson, R. Simha, J.D. McGervey, T.R. Maier, A.F. Halasa, H. Ishida, Positron annihilation lifetime studies of changes in free volume on cross-linking cis-polyisoprene, high-vinyl polybutadiene, and their miscible blends, J. Polym. Sci. Part B Polym. Phys. 37 (1999) 2754–2770, https://doi.org/10.1002/(SICI)1099-0488(19991001)37.
[11] H. Ismail, S. Tan, B.T. Poh, Curing and mechanical properties of nitrile and natural rubber blends, J. Elastomers Plast. 33 (4) (2001) 251–262, https://doi.org/10.1106/DQN6-QXA0-UC3W-U45H.
[12] A.A. Galuska, R.R. Poulter, K.O. McElrath, Force modulation AFM of elastomer blends: morphology, fillers and cross-linking, Surf. Interface Anal. 25 (6) (1997) 418–429, https://doi.org/10.1002/(SICI)1096-9918(199706)25:6<418::AID−SIA253>3.0.CO,2-P.
[13] M.J.R. Loadman, A.J. Tinker, The application of swollen-state CW-1H NMR spectroscopy to the estimation of the extent of crosslinking in vulcanized polymer blends, Rubber Chem. Technol. 62 (2) (1989) 234–245, https://doi.org/10.5254/1.3536242.
[14] P.S. Brown, A.J. Tinker, Factors affecting the NMR technique for estimation of crosslink density in rubber blends, J. Nat. Rubber Res. 5 (4) (1990) 286–295.
[15] P.S. Brown, M. John, R. Loadman, A.J. Tinker, Applications of FT-NMR to crosslink density determinations in natural rubber blend vulcanizates, Rubber Chem. Technol. 65 (4) (1992) 744–760, https://doi.org/10.5254/1.3538639.
[16] A.J. Tinker, Distribution of Crosslinks in Vulcanized Blends, Rubber Chem. Technol. 68 (3) (1995) 461–480, https://doi.org/10.5254/1.3538751.
[17] A. Karekar, K. Oßwald, K. Reincke, B. Langer, K. Saalwächter, NMR studies on the phase-resolved evolution of cross-link densities in thermo-oxidatively aged elastomer blends, Macromolecules 53 (24) (2020) 11166–11177, https://doi.org/10.1021/acs.macromol.0c01614.
[18] B. Klei, J.L. Koenig, NMR imaging of the competitive vulcanization of natural rubber and polybutadiene blends, Acta Polym. 48 (5–6) (1997) 199–207, https://doi.org/10.1002/actp.1997.010480505.
[19] M.D. Ellul, A.H. Tsou, W. Hu, Crosslink densities and phase morphologies in thermoplastic vulcanizates, Polymer 45 (10) (2004) 3351–3358, https://doi.org/10.1016/j.polymer.2004.03.029 (Guildf).
[20] M. Aluas, C. Filip, Solid-state NMR characterization of cross-linking in EPDM/PP blends from 1H –13C polarization transfer dynamics, Solid State Nucl. Magn. Reson. 27 (2005) 165–173, https://doi.org/10.1016/j.ssnmr.2004.10.001.
[21] P. Sotta, C. Fülber, D.E. Demco, B. Blümich, H.W. Spiess, Effect of residual dipolar interactions on the NMR relaxation in cross-linked elastomers, Macromolecules 29 (19) (1996) 6222–6230, https://doi.org/10.1021/ma960141e.
[22] M. Schneider, L. Gasper, D.E. Demco, B. Blümich, Residual dipolar couplings by 1H dipolar-encoded longitudinal magnetization, double- and triple-quantum nuclear magnetic resonance in cross-linked elastomers, J. Chem. Phys. 111 (1) (1999) 402, https://doi.org/10.1063/1.479291.
[23] T. Dollase, R. Graf, A. Heuer, H.W. Spiess, Local order and chain dynamics in molten polymer blocks revealed by proton double-quantum NMR, Macromolecules 34 (2) (2001) 298–309, https://doi.org/10.1021/MA0013915.
[24] K. Saalwächter, B. Herrero, M.A. López-Manchado, Chain order and cross-link density of elastomers as investigated by proton multiple-quantum NMR, Macromolecules 38 (23) (2005) 9650–9660, https://doi.org/10.1021/ma051238g.
[25] I. Syed, G. Hempel, K. Saalwächter, P. Stratmann, M. Klüppel, Entanglements, defects, and Inhomogeneities in nitrile butadiene rubbers: macroscopic versus microscopic properties, Macromolecules 49 (23) (2016) 9004–9016, https://doi.org/10.1021/acs.macromol.6b01802.
[26] K. Saalwächter, P. Ziegler, O. Spyckerelle, B. Haidar, A. Vidal, J.U. Sommer, 1H Multiple-quantum nuclear magnetic resonance investigations of molecular order distributions in poly(Dimethylsiloxane) networks: evidence for a linear mixing law in bimodal systems, J. Chem. Phys. 119 (6) (2003) 3468–3482, https://doi.org/10.1063/1.1589000.
[27] J. Baum, A. Pines, NMR studies of clustering in solids, J. Am. Chem. Soc. 108 (24) (1986) 7447–7454, https://doi.org/10.1021/ja00284a001.
[28] M.K. Dibbanti, M. Mauri, L. Mauri, G. Medaglia, R. Simonutti, Probing small network differences in sulfur- cured rubber compounds by combining nuclear magnetic resonance and swelling methods, J. Appl. Polym. Sci. 132 (1–8) (2015) 42700, https://doi.org/10.1002/app.42700.
[29] M.A. Mansilla, J.L. Valentín, M.A. López-Manchado, A. González-Jiménez, A. J. Marzocca, Effect of entanglements in the microstructure of cured NR/SBR blends prepared by solution and mixing in a two-roll mill, Eur. Polym. J. 81 (2016) 365–375, https://doi.org/10.1016/j.eurpolymj.2016.06.023.
[30] A. Karekar, R. Pommer, B. Prem, C. Czibula, C. Teichert, G. Trimmel, K. Saalwächter, NMR-based cross-link densities in EPDM and EPDM/ULDPE blend materials and correlation with mechanical properties, Macromol. Mater. Eng. 307 (7) (2022), 2100968, https://doi.org/10.1002/MAME.202100968.

[31] K. Saalwächter, F. Lange, K. Matyjaszewski, C.F. Huang, R. Graf, BaBa-Xy16: robust and broadband homonuclear DQ Recoupling for applications in rigid and soft solids up to the highest MAS frequencies, J. Magn. Reson. 212 (1) (2011) 204–215, https://doi.org/10.1016/j.jmr.2011.07.001.
[32] R.P. Brown, T. Butler, S.W. Hawley, Ageing of Rubber - Accelerated Heat Ageing Test Results, Smithers Rapra Technology, 2001.
[33] R.P. Brown, T. Butler, S.W. Hawley, Ageing of Rubber - Accelerated Weathering and Ozone Test Results, Smithers Rapra Technology, 2001.
[34] J. Crabtree, A.R. Kemp, Weathering of soft vulcanized rubber, Rubber Chem. Technol. 19 (3) (1946), https://doi.org/10.5254/1.3557514.
[35] M. Chyasnavichyus, S.L. Young, V.V. Tsukruk, Probing of polymer surfaces in the viscoelastic regime, Langmuir 30 (35) (2014) 10566–10582, https://doi.org/10.1021/LA404925H.
[36] A. Maus, C. Hertlein, K. Saalwächter, A robust proton NMR method to investigate hard/soft ratios, crystallinity, and component mobility in polymers, Macromol. Chem. Phys. 207 (13) (2006) 1150–1158, https://doi.org/10.1002/MACP.200600169.
[37] A. Wittmer, R. Wellen, K. Saalwächter, K. Koschek, Moisture-mediated self-healing kinetics and molecular dynamics in modified polyurethane urea polymers, Polymer 151 (2018) 125–135, https://doi.org/10.1016/j.polymer.2018.07.059 (Guildf).
[38] K. Saalwächter, Proton multiple-quantum NMR for the study of chain dynamics and structural constraints in polymeric soft materials, Prog. Nucl. Magn. Reson. Spectrosc. 51 (1) (2007) 1–35, https://doi.org/10.1016/j.pnmrs.2007.01.001.
[39] K. Saalwächter, M. Klüppel, H. Luo, H. Schneider, Chain order in filled SBR elastomers: a proton multiple-quantum NMR study, Appl. Magn. Reson. 27 (3–4) (2004) 401–417, https://doi.org/10.1007/BF03166740.
[40] L. Jakisch, M. Garaleh, M. Schäfer, A. Mordvinkin, K. Saalwächter, F. Böhme, Synthesis and structural NMR characterization of novel PPG/PCL conetworks based upon heterocomplementary coupling reactions, Macromol. Chem. Phys. 219 (3) (2018) 1–9, https://doi.org/10.1002/macp.201700327.
[41] W. Chassé, J.L. Valentín, G.D. Genesky, C. Cohen, K. Saalwächter, Precise dipolar coupling constant distribution analysis in proton multiple-quantum NMR of elastomers, J. Chem. Phys. 134 (4) (2011), https://doi.org/10.1063/1.3534856.
[42] L. Audouin, V. Langlois, J. Verdu, J.C.M. de Bruijn, Role of oxygen diffusion in polymer ageing: kinetic and mechanical aspects, J. Mater. Sci. 29 (3) (1994) 569–583, https://doi.org/10.1007/BF00445968.
[43] J. Zhi, Q. Wang, M. Zhang, Z. Zhou, A. Liu, Y. Jia, Coupled analysis on hyper-viscoelastic mechanical behavior and macromolecular network alteration of rubber during thermo-oxidative aging process, Polymer 171 (2019) 15–24, https://doi.org/10.1016/J.POLYMER.2019.03.029 (Guildf).
[44] M. Kano, Y. Ohtake, T. Yamanobe, H. Uehara, Effect of water spray on degradation of styrene-butadiene-rubber during accelerated weathering tests, Polym. Degrad. Stab. 182 (2020), 109379, https://doi.org/10.1016/j.polymdegradstab.2020.109379.
[45] K.A.M. Dos Santos, P.A.Z. Suarez, J.C Rubim, Photo-degradation of synthetic and natural polyisoprenes at specific UV radiations, Polym. Degrad. Stab. 90 (1) (2005) 34–43, https://doi.org/10.1016/j.polymdegradstab.2005.01.038.
[46] G.Y. Li, J.L. Koenig, FT-IR Imaging of the thermal oxidation of polyisoprene (PI) rubber at high temperature, Appl. Spectrosc. 56 (11) (2002) 1390–1396, https://doi.org/10.1366/00037020260377670.
[47] G. Martínez-Barrera, H. López, V.M. Castaño, R. Rodríguez, Studies on the rubber phase stability in gamma irradiated polystyrene-SBR blends by using FT-IR and Raman spectroscopy, Radiat. Phys. Chem. 69 (2) (2004) 155–162, https://doi.org/10.1016/S0969-806X(03)00452-3.
[48] A. Zanchet, L.N. Carli, M. Giovanela, R.N. Brandalise, J.S. Crespo, Use of styrene butadiene rubber industrial waste devulcanized by microwave in rubber composites for automotive application, Mater. Des. 39 (2012) 437–443, https://doi.org/10.1016/J.MATDES.2012.03.014.
[49] H.J. Butt, B. Cappella, M. Kappl Force measurements with the atomic force microscope: technique, interpretation and applications, North-Holland, 2005, Vol. 59. 10.1016/J.SURFREP.2005.08.003.
[50] B. Cappella, D. Silbernagl, Nanomechanical properties of polymer thin films measured by force–distance curves, Thin Solid Films 516 (8) (2008) 1952–1960, https://doi.org/10.1016/J.TSF.2007.09.042.
[51] W. Wang, T. Peijs, A.H. Barber, Indentation induced solid state ordering of electrospun polyethylene oxide fibres, Nanotechnology 21 (3) (2009), 035705, https://doi.org/10.1088/0957-4484/21/3/035705.
[52] K.T. Gillen, R.L. Clough, Rigorous experimental confirmation of a theoretical model for diffusion-limited oxidation, Polymer 33 (20) (1992) 4358–4365, https://doi.org/10.1016/0032-3861(92)90280-A (Guildf).
[53] W. Hofmann, Rubber Technology Handbook, Hanser Publishers, Munich, 1989, 1st.
[54] A.S. Aprem, K. Joseph, S. Thomas, Recent developments in crosslinking of elastomers, Rubber Chem. Technol. 78 (3) (2005) 458–488, https://doi.org/10.5254/1.3547892.
[55] N.J. Morrison, M. Porter, Temperature effects on the stability of intermediates and crosslinks in sulfur vulcanization, Rubber Chem. Technol. 57 (1) (1984) 63–85, https://doi.org/10.5254/1.3536002.
[56] 1st A.J. Tinker, K.P. Jones, Blends of Natural Rubber Novel Techniques for Blending with Speciality Polymers, Chapman & Hall, London, 1998, 1st.
[57] H. Dong, Y. Luo, J. Lin, J. Bai, Y. Chen, B. Zhong, D. Jia, Effects of modified silica on the Co-vulcanization kinetics and mechanical performances of natural rubber/styrene–butadiene rubber blends, J. Appl. Polym. Sci. 48838 (2019) 1–9, https://doi.org/10.1002/app.48838.